Global Potential Energy Surface Exploration of In-Ga-Zn-O (IGZO) Reveals Ga-rich Layered Channel Material

Yi-Fan Hu,[1] Ji-Li Li,[1] Zhixin Guo,[2] Zhi-Pan Liu[1,*] and Ye-Fei Li[1,*]

[1]Collaborative Innovation Center of Chemistry for Energy Material, Shanghai Key Laboratory of Molecular Catalysis and Innovative Materials, Key Laboratory of Computational Physical Science, Department of Chemistry, Fudan University, Shanghai 200433, China
[2] State Key Laboratory for Mechanical Behavior of Materials and School of Materials Science and Engineering, Xi'an Jiaotong University, Xi'an, Shanxi 710049, China

ABSTRACT. C-axis aligned Crystalline indium-gallium-zinc oxides (CAAC-IGZOs) with layered phase are widely utilized as functional tunnel material for thin-film transistors (TFTs). Their performance, i.e. stability or mobility etc., of IGZO strongly depend on the Indium:Gallium:Zinc (In:Ga:Zn) ratio, yet most of reports limit to the simplest 1:1:1 ratio for the great difficulty to explore comprehensively the Quaternary IGZO material at all possible contents. Herein by developing a quaternary In-Ga-Zn-O global neural network potential we searched for the full energy landscape with 137 compositions for IGZO, based on which the thermodynamic stable composition range is revealed to be in a general formula of $(In_xGa_{2-x}ZnO_4)_m(ZnO)_n$ with $0.5<x<1.5$, $m > 1$ and n as a non-negative integer. Importantly, we screened out 15 stable CAAC-IGZO candidates with favorable thermal and optical stability. Their electrical properties and device simulation are verified by density functional theory (DFT) calculations. Our results showed that apart from IGZO(1:1:1), a Ga-rich IGZO(3:5:4) phase can also have similar electrical properties (bandgap ~2.8 eV, effective mass ~0.26 m_0) and favorable properties with subthreshold swing being 82 meV/dec in simulated 6-nm device, respectively, superior to IGZO(1:1:1) 88 meV/dec.

I. INTRODUCTION

Indium-gallium-zinc oxide (IGZO) materials emerge as a cornerstone material for thin-film transistors (TFTs) utilized in high-performance display technologies including liquid crystal displays (LCDs) and organic light-emitting diodes (OLEDs) [1]. Depending on In:Ga:Zn ratio, IGZO can have either spinel or layered crystalline structures, where the layered structures [2] with In:Ga=1:1, e.g. $InGaO_3(ZnO)_5$ and $InGaO_3(ZnO)_3$ with alternating InO_2, $GaZnO_2$ and ZnO layers, demonstrate superior carrier mobility (>10 $cm^2/V{\cdot}s$), ultralow off-state leakage currents (<10^{-15} A/μm), wide optical bandgap (>3 eV), and excellent environmental stability, surpassing those of amorphous IGZO or conventional Si-based semiconductors [3–7]. The layered IGZO can now be fabricated via magnetron sputtering [8,9] or plasma enhanced atomic layer deposition [10] method, which can obtain C-axis-aligned crystalline IGZO (CAAC-IGZO) at relatively low temperature (300 °C) and In:Ga:Zn ratio of 1:1:1 is the composition widely tested in experiments [12–18].

It was however found that In:Ga:Zn ratio in CAAC-IGZO critically influences the electrical performance [7,18], for example, it is reported by Semiconductor Energy Laboratory Co. that field-effect mobility (μ_{FE}) of In-rich CAAC-IGZO (4:2:3) (μ_{FE}=15.1cm^2/V^{-s}) over-performs the conventional IGZO with ratio of 1:1:1 (μ_{FE} ~ 7.5cm^2/V^{-s}) [19,20]. Additionally, the laboratory also suggested that the increase of Ga or Zn content enable the material to have better electrical stability or structural stability [7]. Therefore, great efforts have been devoted to search In:Ga:Zn compositions to reach higher performance, lower power consumption, and improved stability, which involves detailed knowledge on the electrical device parameters at different compositions, such as threshold voltage, subthreshold swing, and on-state current at different In:Ga:Zn compositions. Since the precise control over the In:Ga:Zn composition in fabricating IGZO TFTs remains technically challenging due to the complex chemical interactions among these three elements during deposition [18], no comprehensive data on the device performance at different In:Ga:Zn compositions are available to date.

Here with the advent of global neural network (G-NN) potential [21], we are able to explore the full ternary phase diagram for IGZO system using the stochastic surface walking (SSW) global optimization [21–23]. From these data, we identified 15 stable IGZO candidates with negative formation energies (ΔE_f) and positive oxygen vacancy (O_v) formation energies (ΔE_{O_v}). Band structures, partial density of states (PDOS), and carrier transport properties are further investigated on four representative compositions—1:1:1, 1:1:5, 3:5:4, and 5:3:4 via first-principles calculations. Notably, we report that a Ga-rich IGZO composition (In:Ga:Zn = 3:5:4) can be a promising candidate for CAAC-IGZO

*Contact author: yefeil@fudan.edu.cn;
zpliu@ fudan.edu.cn

fabrication, which demonstrates good performance in nanoscale TFT simulations.

II. METHODS

A. SSW-NN global optimization

The stochastic surface walking [23] global structural search based on the global neural network potential (SSW-NN) method was applied to search for the global PES exploration of IGZO bulk structures. The SSW-NN method is implemented in large-scale atomic simulation using neural network potential (LASP) [24] code (www.lasphub.com). Here, an In-Ga-Zn-O quaternary G-NN potential is first generated by iterative learning density functional theory (DFT) dataset utilizing the PES structures sampled from the SSW global PES exploration. The finally generated data set contains 58,572 structures including bulk, surface, and interfaces with various In, Ga, Zn, O compositions. The In-Ga-Zn-O quaternary G-NN potential has 481 power-type structure descriptors (PTSDs) for each element (276 two-body 165 three-body and 40 four-body PTSDs), obtaining the root-mean-square error (RMSE) for energy and force of 4.787 meV/atom and 0.122 eV/Å (Table S1), which is adequate to distinguish the low energy minima IGZO (The benchmark of G-NN calculations against DFT results is tabulated in Table S2). The G-NN calculations reach more than four orders of magnitude speed-up compared to DFT calculations, enabling the highly efficient global PES sampling to identify low-energy crystalline structures. All low-energy structures obtained from SSW-NN were further verified using DFT calculations (see below Section IIB) and all energetics reported in this work without explicitly mentioning are from DFT.

B. DFT calculations

All energies reported in this work are from DFT calculations using the plane-wave Vienna Ab-initio simulation package (VASP) [25]. The electron-ion interaction is represented by projector-augmented wave (PAW) potential [26,27] and the kinetic cutoff was set as 450 eV. The first Brillouin zone k-points were sampled using the Monkhorst-Pack scheme with an automated mesh determined by 25 times reciprocal lattice vectors [28]. The exchange-correlation function employed was GGA-PBE [29], and the hybrid DFT calculations with the HSE06 [30] functional were also utilized to describe the band structure.

C. In-Ga-Zn ternary phase diagram, thermodynamic convex hull, and formation energy of oxygen vacancy

The In-Ga-Zn ternary phase diagram is constructed using formation energies (ΔE_f) of various IGZO compositions with the following equation:

$$\Delta E_f = \frac{\left(E_{IGZO} - \frac{x}{2}E_{In2O3} - \frac{y}{2}E_{Ga2O3} - zE_{ZnO}\right)}{x+y+z} \quad (1)$$

Here, the bulk In_2O_3, Ga_2O_3, and ZnO are used as references. E_{IGZO} is the energy of a stoichiometric IGZO with a general formula of $In_xGa_yZn_zO_{[1.5(x+y)+z]}$. The content of O atoms is set to keep the formal charge of In^{3+}, Ga^{3+}, and Zn^{2+}. For simplicity, we use the term $In_xGa_yZn_z$ to denote the chemical compositions of IGZO, and the contents of In, Ga, Zn are defined as $\frac{A}{x+y+z}$, where A represents either x, y, or z.

The thermodynamic convex hull diagram along the In: Ga = 1: 1 line is calculated using Eq. (2):

$$\Delta E = \frac{\left(E_{IGZO} - yE_{ZnO} - xE_{InGaO_3}\right)}{x+y} \quad (2)$$

where ZnO and $InGaO_3$ (the endpoints of the line) are used as references.

The formation energy of oxygen vacancy (O_v) is calculated by

$$\Delta E_{O_v} = E_{IGZO-O_v} - E_{IGZO} + \mu_O \quad (3)$$

where the E_{IGZO} is the total energy of bulk IGZO, E_{IGZO-O_v} is the IGZO bulk structure with an O_v, and μ_O is the chemical potential of O. The latter is derived from the energy required to remove an oxygen atom from reference In_2O_3, a standard justified by experimental synthesis conditions where In_2O_3, ZnO and Ga_2O_3 coexist. Among these, In_2O_3 exhibits the lowest O_v formation energy, making it the logical basis for defining μ_O.

D. Electronic Transport Simulations

The electronic transport simulations were performed by DFT calculations coupled with the nonequilibrium Green function (NEGF), implemented in the Quantum Atomistix ToolKit (QuamtumATK) package [31]. The PseudoDojo pseudopotential with medium accuracy is employed, which is proved to be adequate for device transport calculation [32]. The k-points of the device are set to $4 \times 1 \times 150$ and the temperature is set as 300K.

*Contact author: yefeil@fudan.edu.cn;
zpliu@ fudan.edu.cn

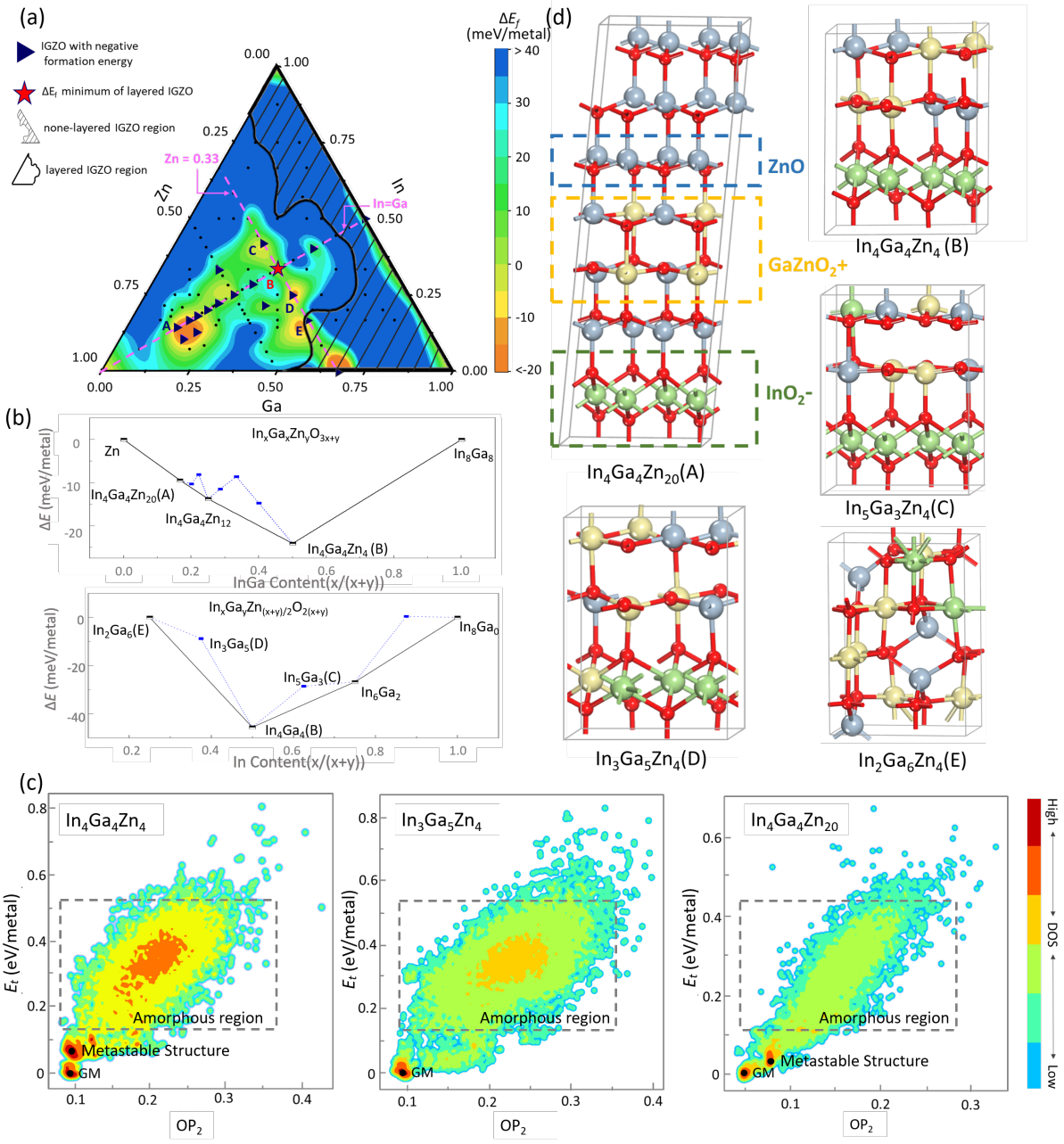

FIG 1. Global PES exploration of IGZO bulk phases. (**a**) Ternary In-Ga-Zn oxide phase diagram. The color represents the formation energy (ΔE_f see Eq.(1)). Each black dot represents a global minimum structure at a given composition. Red star labels $In_4Ga_4Zn_4$ oxide that has the lowest ΔE_f in the layered structure region. Dark blue triangles represent structures with negative ΔE_f, including $In_4Ga_4Zn_{20}$(A), $In_4Ga_4Zn_4$(B), $In_5Ga_3Zn_4$(C), $In_3Ga_5Zn_4$ (D) and $In_2Ga_6Zn_4$(E), which are labeled A-E in panel (a). Compositions outside the shading region are layered structures. (**b**) Convex hull diagrams of IGZO along the In: Ga = 1: 1 and Zn = 0.33 lines. Black squares in the convex hull diagrams represent the convex points. (**c**) Distance-weighted Steinhart OP_2-energy contour plots of the global PES for $In_4Ga_4Zn_4$, $In_3Ga_5Zn_4$ and $In_4Ga_4Zn_{20}$. The y axis is the relative total energy (E_t) per metal atom with respect to the GM. (**d**) Global minimum structures of $In_4Ga_4Zn_{20}$ (A), $In_4Ga_4Zn_4$(B), $In_5Ga_3Zn_4$(C), $In_3Ga_5Zn_4$(D) and $In_2Ga_6Zn_4$(E), respectively. Green balls: I; yellow balls: Ga; grey balls: Zn; red balls: O.

*Contact author: yefeil@fudan.edu.cn;
zpliu@ fudan.edu.cn

III. Results and discussions

A. Thermal Stability of crystalline IGZOs

In order to systematically evaluate the structural configurations and thermal stability of diverse IGZO compositions, we constructed a ternary phase diagram by performing SSW-NN global optimization for a total of 137 compositions across various In: Ga: Zn ratios. For a given composition, its global minimum (GM) is identified from over 15,000 minima obtained from SSW-NN trajectory. The results are shown in Fig 1a, where each dot represents a global minimum (GM) (Details of all examined ratios are provided in Table S3). Compositions with negative formation energies are marked by triangles and highlighted in warmer colors, while those that are not layered crystal structures (not interested in this work) are dark shaded. From Fig 1a, we found that 18 compositions exhibit negative ΔE_f, with the $In_4Ga_4Zn_4$ composition having the lowest formation energy (see Eq. (1), ΔE_f = -36 meV/metal), as indicated by the red star. Specifically, 15 of them are layered structures: a majority of them (9 out of 15) lie along the In: Ga = 1: 1 line, such as $In_4Ga_4Zn_{20}$(A), $In_4Ga_4Zn_4$(B) etc.; and 4 out of 15 compositions locate at another line of Zn=0.33 (dashed lines in Fig 1a), including $In_5Ga_3Zn_4$(C) and $In_3Ga_5Zn_4$(D). The $In_4Ga_4Zn_4$(B) locates at the cross point of the two lines. $In_2Ga_6Zn_4$(E) and Ga_8Zn_4, although on the Zn = 0.33 line with negative ΔE_f, they are spinel type structures, also not interested in this work.

Since most of the structures lies on the two purple dashed lines, to further assess the thermodynamic stability of IGZO, we calculate the thermodynamic convex hull diagram along the In: Ga = 1: 1 line and Zn = 0.33 lines in Fig 1b (see Eq. (2)). The compositions along In: Ga =1: 1 can be represented by a general formula $In_xGa_xZn_yO_{3x+y}$. As shown in the top frame of Fig 1b, where the x-axis, InGa content x/(x+y), labels the contents of $InGaO_3$, there are three extreme points in the thermodynamic convex hull diagram, namely $In_4Ga_4Zn_{12}$, $In_4Ga_4Zn_{20}$, and $In_4Ga_4Zn_4$ (the black squares in Figure 1b), which indicates these compositions are thermodynamically favorable. As for the convex hull along Zn=0.33, the compositions can be expressed by $In_xGa_yZn_{(x+y)/2}O_{2(x+y)}$ and In content can be calculated by x/(x+y) (x-axis). As shown in the bottom frame of Figure 1b, $In_3Ga_5Zn_4$ and $In_5Ga_3Zn_4$ are only 10 meV/metal atom and 5 meV/metal above the solid convex hull lines, which suggest these materials are also likely fabricated in experiment [34]. It can be further deduced that the In: Ga > 3: 1 materials become less stable (>20 meV/metal atom above the convex hull line) and less likely to be fabricated.

*Contact author: yefeil@fudan.edu.cn;
zpliu@ fudan.edu.cn

We also highlighted the global PES of $In_4Ga_4Zn_4$, $In_3Ga_5Zn_4$ and $In_4Ga_4Zn_{20}$ in Fig 1c via E_t-OP contour plot, where E_t is the total energy relative to the GM and OP is the structure fingerprint using the distance weighted Steinhart order parameter with the degree l = 2 (OP_2) [22]. The GM is emphasized by a black dot and, locating at energy zero. We found that when In equals to Ga, $In_4Ga_4Zn_4$ and $In_4Ga_4Zn_{20}$, a metastable crystalline structure with energy close to the GM (<0.08 eV/atom) is present (will be detailed in Section IIIB). This introduces fabrication complexity in obtaining the most stable layer structure. By comparing three global PES contour plots, we noticed that the density of states (DOS) in the amorphous region of $In_4Ga_4Zn_{20}$ is much lower than those in $In_4Ga_4Zn_4$ and $In_3Ga_5Zn_4$, apparently due to the extra ZnO contents. This suggests that the crystalline structure of $In_4Ga_4Zn_{20}$ is more stable and should be easier to synthesize, as indeed observed in experiment [7].

B. Crystal structures of layered IGZO

To gain a deeper understanding on the composition-structure relationship for layered IGZO, we take a close look at six representative compositions: $In_4Ga_4Zn_{20}$, $In_4Ga_4Zn_4$, $In_3Ga_5Zn_4$, $In_5Ga_3Zn_4$, $In_2Ga_6Zn_4$, and Ga_8Zn_4. $In_5Ga_3Zn_4$ is the one with the highest In content among all compositions with ΔE_f < 0 in Fig 1a; Ga_8Zn_4 is the one with the highest Ga content; and $In_4Ga_4Zn_{20}$ has the highest Zn content. The $In_4Ga_4Zn_{20}$, $In_4Ga_4Zn_4$, $In_3Ga_5Zn_4$, $In_5Ga_3Zn_4$ exhibit layered structures characterized by oxygen sublattices arranged in a hexagonal closest packing (hcp) pattern, as shown in Figure 1d (A, C, D, and E atomic structures). In contrast, the $In_2Ga_6Zn_4$ and Ga_8Zn_4 adopt a spinel (non-layered) structure (see Fig 1d, F structure), where the oxygen anions form the cubic close packing sublattice.

The $In_4Ga_4Zn_{20}$ (see Fig 1d, A structure), a #Cm, 8 space group structure, consists of alternating layers of InO_2, $GaZnO_2$, and ZnO (as indicated by the green, yellow, and blue dashed boxes in Fig 1d, A structure), arranged in an ABCA stacking sequence along the c-axis. DFT calculations indicate the Bader atomic charges for In, Ga, Zn and O are 1.82±0.02, 1.82±0.02, 1.25 ± 0.01 and -1.22 ± 0.01, respectively, which suggests that three different layers can be better characterized as InO_2^-, $GaZnO_2^+$ and ZnO. In the InO_2^- layer, In atoms occupy the octahedral vacancies of the oxygen sublattice, with a coordination number (CN) of 6. In the $GaZnO_2^+$ layer, Ga and Zn atoms alternate to occupy the trigonal bipyramidal sites (CN = 5) tetrahedral sites (CN = 4), respectively. If Ga and Zn atoms in the $GaZnO_2^+$ layer are segregated into separate GaO^+ and ZnO layers, the resulting structure

corresponds to a metastable structure in Figure 1c (the structure is shown in Fig S1). Finally, in the ZnO layer, Zn atoms occupy tetrahedral vacancies (CN = 4), similar to that in bulk ZnO. This similarity to ZnO bulk suggests a template effect to drive the formation of layered IGZO structure and explains why $In_4Ga_4Zn_{20}$ has much lower DOS at the amorphous region (Fig 1c).

In contrast, the structure of $In_4Ga_4Zn_4$ (see Fig 1d B) comprises only InO_2^- and $GaZnO_2^+$ layers without any neutral ZnO layers (#P21/C, 14). The configurations of both InO_2^- and $GaZnO_2^+$ layers are analogous to those observed in $In_4Ga_4Zn_{20}$ as previously described. The metastable state (Fig 1c) is also present where the $GaZnO_2^+$ layer is separated into GaO^+ and ZnO sublayers. By comparing the structures between $In_4Ga_4Zn_4$ and $In_4Ga_4Zn_{20}$, it is evident that the Zn content in IGZO should be at least 0.33; otherwise, the Zn content is insufficient to form adequate $GaZnO_2^+$ layers to neutralize the charge of InO_2^-. On the other hand, when the Zn content exceeds one-third, the excess Zn grow into multiple neutral ZnO layers, which effectively decreases the contents of InO_2 layer and should also affect the electronic property of the material.

In-rich $In_5Ga_3Zn_4$ (#P1, 2) (Fig 1d, C structure) composes of alternating InO_2^- and $Ga_{0.75}In_{0.25}ZnO_2^+$ layers. Notably, the $Ga_{0.75}In_{0.25}ZnO_2^+$ layer can be interpreted as one-quarter of Ga atoms within the $GaInZnO_2^+$ layer being replaced by In atoms, suggesting the substitution between Ga and In in $GaZnO_2^+$ layer is energetically feasible, which could be attributed to the fact that both elements possess the +3 formal charge. Since the further increase of the In content would cause ΔE_f turning positive, the upper limit for In content in layered IGZO is therefore 0.42.

On the other hand, for Ga-rich $In_3Ga_5Zn_4$ (#P1, 2), it comprises alternating $In_{0.75}Ga_{0.25}O_2^-$ and $GaZnO_2^+$ layers (see Fig 1d, D structure). Apparently, being contrast to In-rich $In_5Ga_3Zn_4$, one-quarter of In atoms from the InO_2^- layer are now substituted by Ga atoms.

As the Ga content further increases to 0.5 ($In_2Ga_6Zn_4$ (#C2, 5)) or higher (Ga_8Zn_4 (#Fd3m, 227)), their most stable crystal structure changes to the spinel structure (see Fig 1d, E structure), where trivalent In and Ga occupy octahedral sites in the oxygen sublattice, while bivalent Zn occupies the remaining tetrahedral sites. This result indicates that the IGZO with Ga content higher than 0.5 are not feasible to form CAAC-IGZO.

For consistency, we name different layers in all layered IGZO structure hereafter as the In layer ($In_{1-x}Ga_xO_2^-$), Ga layer ($Ga_{1-x}In_xZnO_2^+$), and Zn layer (ZnO).

To summarize above, equivalent number of In layer and Ga layer are required to maintain the overall electrical neutrality, although In and Ga atoms are interchangeable in a small range. The layered IGZO can thus be written as $In_xGa_{2-x}O_3$-$(ZnO)_y$ while the number (y) of neutral Zn layer can vary largely. The Ga and In content controls where the spinel structure or other thermodynamically unfavorable structures are possible to form, as shown in Fig 1a. These further limits the general formula to $(In_xGa_{2-x}ZnO_4)_m(ZnO)_n$, where $0.5 < x < 1.5$, $m > 1$, and n is a non-negative integer. Our results narrow significantly the possible composition range for layered structures of $0.09 < x < 1.23$ that previously reported by Nakamura et al. [2]. Importantly, our convex hull diagram along In = Ga suggests three stable compositions—1:1:1, 1:1:3, and 1:1:5—that have been experimentally synthesized as single-crystalline IGZO [34,35], validating the reliability of our computational predictions. From the global PES of three key compositions (Fig 1c), we demonstrate that (i) nonequivalent In and Ga content prevent the formation of metastable structures with pure GaO^+ and ZnO sublayers; (ii) a large content of ZnO can stabilize the layered crystalline structure by decreasing the formation tendency of amorphous phases.

C. Optical Stability of IGZOs

After we obtained the GM structures for all compositions, we then investigated the defect formation ability of these crystal phases. The formation of oxygen vacancies (O_v) is a crucial factor influencing the long-term reliability and performance of IGZO-based devices, particularly concerning the Negative Bias Illumination Stress (NBIS) instability [36–39]. NBIS instability occurs when IGZO devices are subjected to negative bias under illumination, leading to the degradation of the electrical characteristics, such as threshold voltage shifts, increased leakage current, and decreased switching performance. This instability is primarily attributed to the trapping of charge carriers at defects, notably O_v, under light exposure and negative bias conditions.

To evaluate the resistance to NIBS, we have calculated the formation energy of O_v (ΔE_{O_v}, see Eq. (3)) across 137 various compositions within the In-Ga-Zn ternary phase diagram. Our O_v concentration for all phases is controlled to be around 1.0%. It should be mentioned that all possible oxygen sites for each

*Contact author: yefeil@fudan.edu.cn;
zpliu@ fudan.edu.cn

composition are tested and the one with the lowest ΔE_{O_v} is utilized to construct the contour plot in Figure 2 (All data can be found in SI, Table S4). Table I lists 15 compositions that satisfy $\Delta E_{O_v} > 0$ eV, $\Delta E_f < 0$ eV and have a layered crystal structure, including 8 compositions with equivalent In and Ga (i.e. $In_4Ga_4Zn_4$, $In_4Ga_4Zn_{20}$ etc.); five Ga-rich compositions ($In_3Ga_5Zn_4$, $In_3Ga_5Zn_{16}$, $In_3Ga_5Zn_{20}$, $In_6Ga_{10}Zn_{12}$, and $In_3Ga_5Zn_8$) and two In-rich compositions ($In_5Ga_3Zn_4$ and $In_5Ga_3Zn_{20}$). They are screened out to be promising candidates for channel materials in TFTs (see hollow triangles in Fig 2). From Table I, we noticed that O_v in most compositions favors the Ga-layer or Zn-layer, where Zn is present. This suggests the electrostatic interaction dominates the O_v formation energy since Zn is the lowest charge cation compared to Ga and In. Furthermore, since the In–O bond is easier to break than the Ga–O bond—due to the smaller atomic radius of Ga (1.26 Å) compared to In (1.44 Å) [40]—we observe that in the two In-rich compositions, O_v tends to form near In atoms rather than Ga atoms in the Ga layer.

TABLE I. Formation energy, oxygen sites and first shell atoms of O_v in 15 layered IGZOs (sorted by ΔE_{O_v})

IGZO	ΔE_{O_v} (eV)	O_v Sites (layer)[a]	1st-shell Atoms[b]	Ov (%)
$In_4Ga_4Zn_4$	0.74	Ga	2Ga,2Zn	0.8
$In_4Ga_4Zn_{12}$	0.70	Zn	4Zn	1.0
$In_3Ga_5Zn_{16}$	0.65	Zn	4Zn	0.9
$In_4Ga_4Zn_{16}$	0.63	Zn	4Zn	0.9
$In_3Ga_5Zn_{20}$	0.58	Zn	4Zn	0.8
$In_8Ga_8Zn_4$	0.57	In	Ga,3In	0.9
$In_4Ga_4Zn_{10}$	0.50	Zn	4Zn	0.6
$In_4Ga_4Zn_{14}$	0.48	Ga	2Ga,2Zn	1.0
$In_3Ga_5Zn_4$	0.47	Ga	2Ga,2Zn	0.8
$In_4Ga_4Zn_{20}$	0.44	Ga	2Ga,2Zn	0.7
$In_8Ga_8Zn_{12}$	0.39	Ga	2Ga,2Zn	0.7
$In_6Ga_{10}Zn_{12}$	0.38	Ga	2Ga,2Zn	0.8
$In_3Ga_5Zn_8$	0.30	Ga	Ga,3Zn	0.8
$In_4Ga_2Zn_6$	0.09	Ga	3Zn,In	0.8
$In_5Ga_3Zn_4$	0.00	Ga	3Zn,In	0.6

[a] Ga-layer: $GaZnO_2^+$; Zn-layer: ZnO; In-layer: InO_2^-.
[b] The closest metal atoms (1st-shell) around O_v.

Fig 2 reveals that, in general, the Ga-rich IGZO (In: Ga < 1) exhibits a higher ΔE_{O_v} than that of In-rich IGZO (In: Ga > 1), as evidenced by the warmer color observed in the bottom-right region relative to the top-left region. For instance, ΔE_{O_v} of $In_3Ga_5Zn_4$ is 0.47 eV higher than that of $In_5Ga_3Zn_4$, which can be contributed to the fact that O_v in In_3Ga_5Zn is bonded with more Ga atoms despite both of their O_v locate within Ga-layer.

*Contact author: yefeil@fudan.edu.cn;
zpliu@ fudan.edu.cn

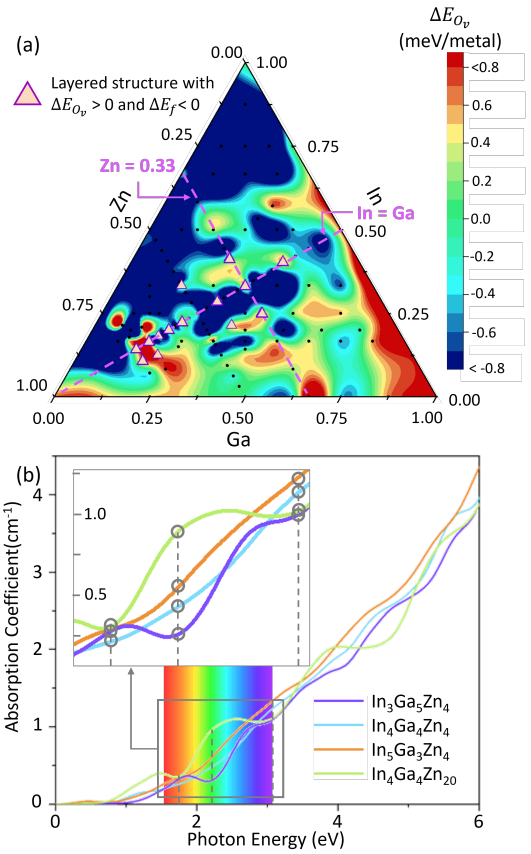

FIG 2. **Oxygen vacancy and optical properties of IGZO.** (**a**) Ternary diagram for formation energies of oxygen vacancies. Compositions with positive ΔE_{O_v} and negative ΔE_f are marked with hollow triangles. (**b**) Optical absorption coefficient of different IGZO compositions with ~1% O_v. The absorption spectra of IGZO within visible light range is enlarged in inset with coefficients at the representative photon energy (red, green and purple light region) being circled.

We calculated the optical absorption coefficient of four representative IGZOs with O_v, i.e. $In_4Ga_4Zn_4$, $In_3Ga_5Zn_4$, $In_5Ga_3Zn_4$, and $In_4Ga_4Zn_{20}$, as shown in Fig 2b. Generally, IGZOs with O_v perform absorption coefficients from 0.25 to 1.40×10^5 cm^{-1} within visible lights range (photon energy 1.65-3.10 eV). To be specific, $In_4Ga_4Zn_4$ absorb least red light (1.75 eV) with absorption coefficient of 0.26 $\times10^5$ cm^{-1} and others around 0.34 $\times10^5$ cm^{-1}; In_4Ga_4Zn absorb green light (2.25 eV) the most with coefficient of 1.02 $\times10^5$ cm^{-1}, followed by In_5Ga_3Zn (0.63 $\times$ 10^5 cm^{-1}), $In_4Ga_4Zn_2$ (0.50 $\times$ 10^5 cm^{-1}), $In_3Ga_5Zn_4$ (0.63 $\times10^5$ cm^{-1}) in sequence; $In_5Ga_3Zn_4$ absorb purple light (3.10 eV) the most with coefficient of 1.33 $\times10^5$ cm^{-1}, followed sequentially by $In_4Ga_4Zn_4$ (1.26 $\times10^5$ cm^{-1}),

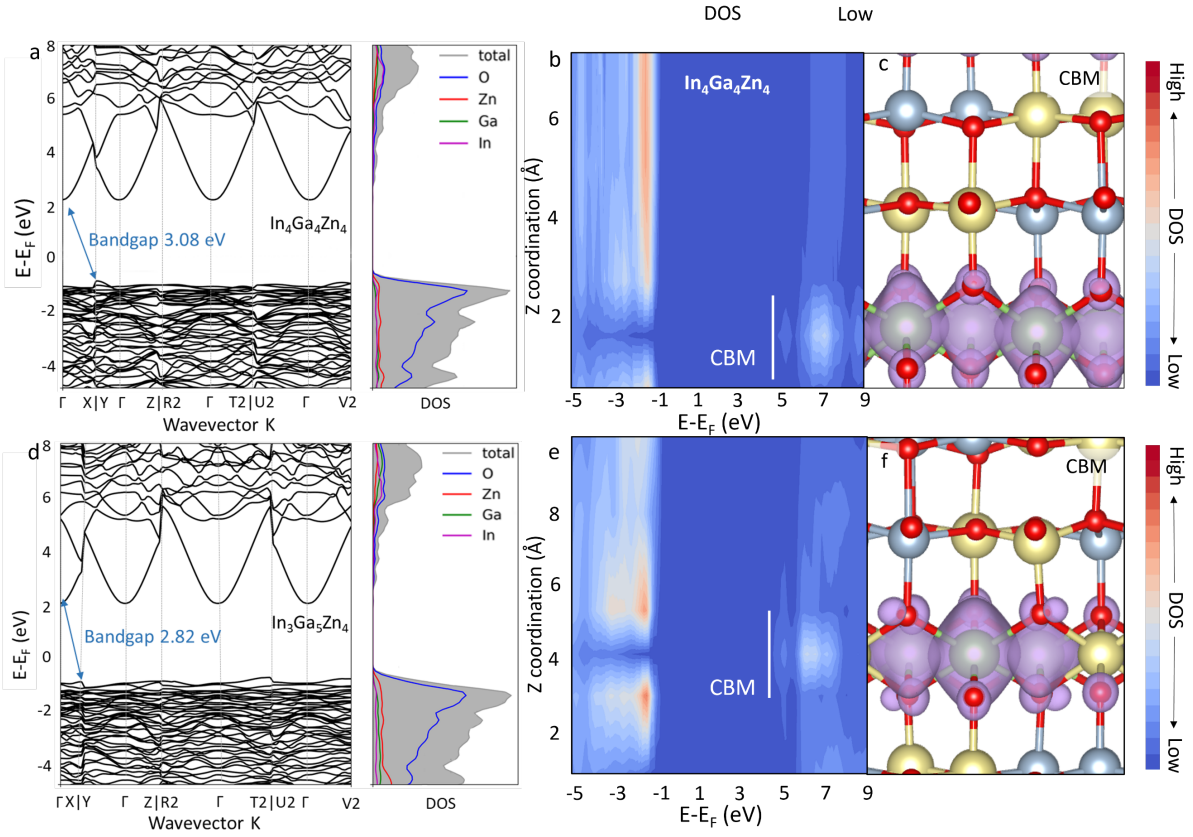

FIG 3. **Electronic structures of IGZOs using HSE06 (a-c)** Band structures, partial density of states (DOS) projected along z coordinate and CBM isosurfaces for $In_4Ga_4Zn_4$. **(d-f)** Band structures, partial density of states (DOS) projected along z coordinate and CBM isosurfaces for $In_3Ga_5Zn_4$.

$In_4Ga_4Zn_{20}$ (1.11×10^5 cm^{-1}), and $In_3Ga_5Zn_4$ (1.02×10^5 cm^{-1}).

By integrating the optical absorption coefficients over the visible light region (i.e., the area under the curve in Fig. 2b), we find that the Ga-rich $In_3Ga_5Zn_4$ exhibits the smallest value, 0.89×10^5, indicating the weakest visible light absorption. The integrated areas increase in the order of $In_4Ga_4Zn_4$ (0.94×10^5), $In_5Ga_3Zn_4$ (1.12×10^5), and $In_4Ga_4Zn_{20}$ (1.28×10^5). These results suggest that under illumination, the Ga-rich $In_3Ga_5Zn_4$ may exhibit greater NBIS instability due to its lower absorption.

D. Electronic structures of four representative IGZO

To provide a basic understanding of the electronic transport properties of IGZO, we then calculated the electronic structures of four representative layered compositions using DFT, i.e., $In_4Ga_4Zn_4$, $In_4Ga_4Zn_{20}$, $In_5Ga_3Zn_4$, and $In_3Ga_5Zn_4$, whose results are visualized in Fig 3a-c, Fig 3d-f, Fig S2, and Fig S3, respectively. Among them, $In_4Ga_4Zn_4$ has the largest band gap of 3.08 eV, and it is ~2.8 eV for other compositions. All materials have low carrier mass, being less than 0.26 m_0, indicating the high carrier mobility. These four compositions, although at different In: Ga ratio, all exhibit promising electronic conductivity.

The calculated electronic structure for $In_4Ga_4Zn_4$ is shown in Figure 3a-c. Band structure in Fig 3a reveals that $In_4Ga_4Zn_4$ is an indirect, n-type semiconductor, that is, carrier (electron) transport via CBM, whose effective mass is calculated to be 0.25 m_0. From projected-density-of-states (PDOS) distribution along z coordinate and isosurface of CBM, as shown in Fig 3b-c, we can assign $In_4Ga_4Zn_4$'s CBM position mainly locating at the In-layer.

Similar to $In_4Ga_4Zn_4$, the band structure of $In_3Ga_5Zn_4$, $In_5Ga_3Zn_4$ and $In_4Ga_4Zn_{20}$ also suggest them to be n-type, indirect semiconductors, as shown in Fig 3d, Fig S2a and Fig S3b. Consistently, their CBMs all locate mainly at the In-layer (see Fig 3e,f, Fig S2b,c and Fig S3b,c). Notably, in $In_3Ga_5Zn_4$, Ga's existence at In-layer appear to interrupt the continuous

*Contact author: yefeil@fudan.edu.cn;
zpliu@ fudan.edu.cn

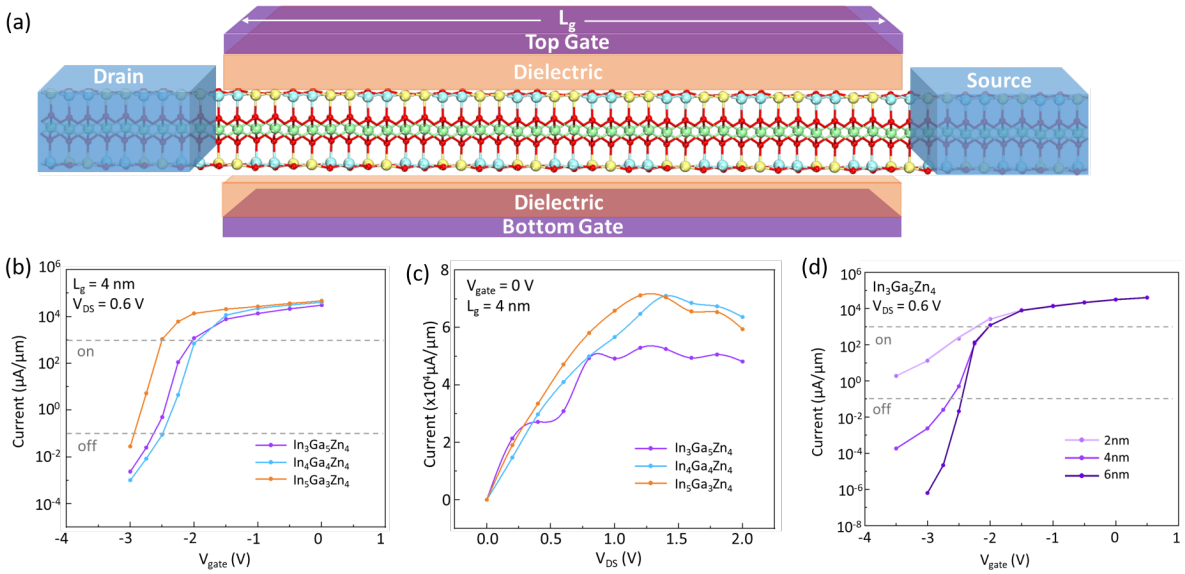

FIG 4. **Devic simulation of IGZO-based transistors.** (a) Device model with IGZO as the channel material. $In_4Ga_4Zn_4$ is shown as example. Blues boxes in the left and right end are drain and source, respectively. Purple boxes on the top and bottom stand for the gate. Orange boxes represent the dielectric. (b) Transfer characteristic curves of three different IGZO channels with gate length (L_g) of 4 nm. (c) Output characteristic curves of IGZOs with gate length of 4 nm. (d) Transfer characteristic curves of $In_3Ga_5Zn_4$ with gate length of 2 nm, 4 nm, and 6 nm.

channel formed by In atoms, Fig 3f, while, by contrast, the existence of In atom at Ga-layer in $In_5Ga_3Zn_4$ provides extra distribution of CBM in Ga-layer, Fig S2c. For $In_4Ga_4Zn_{20}$ with thick ZnO layers, we found that ZnO layers contribute negilibly to CBM (see Fig S3c), suggesting ZnO is largely a structure stablizer of the material.

In summary, layered IGZO materials are n-type semiconductors and the electrons transport occurs through In-layer, where CBM locates. This phenomenon can be attributed to the diffusive nature of In atoms' 5s orbitals [41] which leads to substantial orbital overlap (Fig 3c and 3f) and form an efficient channel for electron transport. Ga-layer may provide additional channel for electron conduction in In-rich $In_5Ga_3Zn_4$ due to the In's presence in Ga-layer. Zn-layer, in contrast, have no influence on electron transport.

E. Electronic transport of IGZOs

Device simulations were then performed to evaluate the transport properties of various IGZO-based TFTs. Performance criteria were established based on the International Technology Roadmap for Semiconductors (ITRS), which defines high-performance devices as those with an off-current (I_{off}) of $\leq 10^{-1}$ μA/μm and an on-current (I_{on}) of $\geq 10^{3}$ μA/μm [23]. In the simulations, we took (001) slab models with (p2×2) periodicity and Ga-layer as surface termination, whose surface energy is the lowest (< 0.3 J/m²) compared to other possibilities (Table S5). To further determine the rational thickness for our models, we examined the PDOS projected on the c-axis of the IGZO slabs with varying thicknesses—specifically, 2 nm, 4 nm, and 8 nm—as illustrated in Fig S6 and no significant difference are found with respect to the bulk material, suggesting the thickness of the IGZO slabs has a negligible impact on the electronic structure. Based on above analysis, we constructed a device model [42,43] featuring a monolayer, Ga-layer-exposed IGZO as channel material, doped IGZO as electrodes, characterized by gate length (L_g) of 2nm, 4nm and 6nm, as shown in Fig 4a. The dielectric regions are represented with a dielectric constant of $\epsilon = 22\ \epsilon_0$ and have a thickness of 0.4 nm. Two-probe gates, each with a thickness of 0.2nm, are added to fully cover the dielectric regions. Simulations were performed with DFT calculations combined with the NEGF method (see Section II Methods D).

The transfer characteristic curves of $In_4Ga_4Zn_4$, $In_5Ga_3Zn_4$, and $In_3Ga_5Zn_4$ channels (L_g = 4nm) are shown in Fig 4b. When the channel length of 4 nm and drain-source voltage (V_{DS}) of 0.6 V, the gate voltages (V_{gate}) required to turn off the devices (i.e., to achieve an off-current of 10^{-1} μA/μm) are determined to be -2.5 V, -2.6 V, and -2.9 V for $In_4Ga_4Zn_4$, $In_3Ga_5Zn_4$, and $In_5Ga_3Zn_4$, respectively. Concurrently, the gate voltages required to turn the devices on (i.e., to reach

*Contact author: yefeil@fudan.edu.cn;
zpliu@ fudan.edu.cn

an on-current of 10^3 μA/μm) are -1.9 V, -2.0 V, and -2.5 V. $In_4Ga_4Zn_4$ requires the least negative gate voltage, followed closely by $In_3Ga_5Zn_4$, while $In_5Ga_3Zn_4$ requires a significantly more negative gate voltage to turn off/on the device. The subthreshold swing (SS), another key indicator of device efficiency in switching properties (slope of the curve of the linear region), is calculated to be 150, 150, and 100 mV/dec for 4-nm $In_4Ga_4Zn_4$, $In_3Ga_5Zn_4$, and $In_5Ga_3Zn_4$, respectively. As the tunnel increases to 6nm, this value can be further reduced to 88mV/dec, 82 mV/dec and 74 mV/dec, which is close to be the fundamental limit of 60 mV/dec for field effect transistor, termed Boltzmann's tyranny [42]. Comparing to the popular nanoscale MoS_2 and Si-based transistors that have SS values of ~65 mV/dec [42,44] and 100 mV/dec [45], respectively, the layered-IGZO-based devices demonstrate top-gear switching ability. We notice that the previously reported CAAC-IGZO (~100 mV/dec) are measured with channel length more than 30 nm [13,17].

Figure 4c shows the output characteristic curve of 4-nm $In_4Ga_4Zn_4$, $In_3Ga_5Zn_4$, and $In_5Ga_3Zn_4$. For low V_{DS} (below 0.20 V), $In_3Ga_5Zn_4$ exhibits the highest current, 2.1×10^4 μA/μm at 0.20 V and less than 1.95×10^4 μA/μm for others. As V_{DS} increases within the range of 0.20 to 0.80 V, $In_5Ga_3Zn_4$ surpasses $In_3Ga_5Zn_4$ and $In_4Ga_4Zn_4$ in current. Beyond V_{DS} of 0.80 V, $In_3Ga_5Zn_4$ reaches a plateau, where the current stabilizes around 5×10^4 μA/μm, signaling the onset of current saturation. On the other hand, $In_5Ga_3Zn_4$ and $In_4Ga_4Zn_4$ continue to increase their current, peaking at ~7.1×10^4 μA/μm at V_{DS} 1.2 and 1.4 V, respectively. Their on-currents are comparable to previous experimental study that an IGZO transistor with channel length of 100 nm reaches an on-current of 6.5×10^4 μA/μm at V_{DS} 2.7 V and V_g 1.0 V [13]. Additionally, the result that $In_5Ga_3Zn_4$ has higher current aligns with previous experimental studies, which report that IGZO(4:2:3), a composition similar to our 5:3:4, has enhanced field-effect mobility and a more negative threshold voltage [7].

For $In_3Ga_5Zn_4$ channel, we also investigated the impact of channel length on device's transfer characteristic curves with L_g at 2 nm, 4 nm, and 6 nm. The results are shown in Fig 4d. We found that for a 2 nm $In_3Ga_5Zn_4$, it fails to fully turn off within the gate voltage range of -3.5 V to 0 V. As the channel length increases further, the V_{gate} to turn off the device appears above -3.5 V, which is -2.6 V for the 4 nm channel and -2.4 V for the 6nm channel. This is consistent with the reduction in the SS from 150 mV/dec for the 4 nm channel to 82 mV/dec for the 6 nm channel. These results can be understood as the short-channel effects, where too-short channel cannot effectively switch off the device due to quantum tunneling, electron scattering.

V. CONCLUSIONS and REMARKS

To identify high performance IGZO materials for TFT applications, this work develops quaternary In-Ga-Zn-O G-NN potential and explore exhaustively all compositions using SSW global optimization. This leads to the general formula for the stable, low-defect content, layered IGZO, i.e $(In_xGa_{2-x}ZnO_4)_m(ZnO)_n$, where x is in the range of 0.5 to 1.5, m > 1 and n is a non-negative integer. Within this range, we identify a Ga-rich $In_3Ga_5Zn_4$ absorbs visible light the least so as to resist NIBS the best to obtain better optical stability. By performing channel device simulation, we show that $In_3Ga_5Zn_4$ reaches an on-current of 5.0×10^4 μA/μm at V_{DS} 0.8 V and V_{gate} 0V; SS of 82 mV/dec with 6-nm channel length at V_{DS} 0.6 V, being highly competitive to known channel materials. This work establishes a general theoretical framework in searching for the optimum multiple-elements material for a target function, which should be able to reduce tremendously the trial-and-error experimental tests.

ACKNOWLEDGMENTS

This work received financial support from the National Science Foundation of China (12188101, 22033003, 22122301, 92472113), the Fundamental Research Funds for the Central Universities (20720250005, 20720220011), the National Key Research and Development Program of China (2022YFA1503503, 2024YFA1509600), Science & Technology Commission of Shanghai Municipality (2024ZDSYS02), the Natural Science Foundation of Shanghai (24ZR1405100), the Huawei Technologies Co., Ltd., and the Tencent Foundation for XPLORER PRIZE.

SUPPLEMENTAL MATERIAL

We provide supplemental material that includes training dataset of G-NN potential (Table S1, Table S2), comprehensive ΔE_f (Table S3) and ΔE_{O_v} data (Table S4) of calculated structures. Surface energy of IGZOs are tabulated in Table S5. Further atomic structures, band structures and PDOS plots of various IGZO bulk or slab models are also offered (Fig S1-6).

[1] Y. Zhu, Y. He, S. Jiang, L. Zhu, C. Chen, and Q. Wan, Indium–gallium–zinc–oxide thin-film transistors: Materials, devices, and applications, J. Semicond. **42**, 031101 (2021).

*Contact author: yefeil@fudan.edu.cn;
zpliu@ fudan.edu.cn

[2] M. Nakamura, N. Kimizuka, and T. Mohri, The phase relations in the In2O3□Ga2ZnO4□ZnO system at 1350°C, Journal of Solid State Chemistry **93**, 298 (1991).
[3] W. Xu, H. Li, J.-B. Xu, and L. Wang, Recent Advances of Solution-Processed Metal Oxide Thin-Film Transistors, ACS Appl. Mater. Interfaces **10**, 25878 (2018).
[4] Y. Kang, W. Lee, J. Kim, K. Keum, S.-H. Kang, J.-W. Jo, S. K. Park, and Y.-H. Kim, Effects of crystalline structure of IGZO thin films on the electrical and photo-stability of metal-oxide thin-film transistors, Materials Research Bulletin **139**, 111252 (2021).
[5] G. Yan et al., Mechanism Analysis of Ultralow Leakage and Abnormal Instability in InGaZnO Thin-Film Transistor Toward DRAM, IEEE Transactions on Electron Devices **69**, 2417 (2022).
[6] S. Subhechha et al., *Ultra-Low Leakage IGZO-TFTs with Raised Source/Drain for Vt > 0 V and Ion > 30 μA/Mm*, in *2022 IEEE Symposium on VLSI Technology and Circuits (VLSI Technology and Circuits)* (2022), pp. 292–293.
[7] S. Yamazaki and N. Kimizuka, *Physics and Technology of Crystalline Oxide Semiconductor CAAC-IGZO*, 1st ed. (John Wiley & Sons, Ltd, 2016).
[8] S. Yamazaki et al., Back-channel-etched thin-film transistor using c-axis-aligned crystal In–Ga–Zn oxide, Journal of the Society for Information Display **22**, 55 (2014).
[9] J. Y. Cho, J. Jo, P. R. Patil, Y. T. Kim, D.-Y. Cho, J. H. Kim, and J. Heo, Optimization of Sputtering Parameters and Their Effect on Structural and Electrical Properties of CAAC-IGZO Thin-Film Transistors, Electron. Mater. Lett. **20**, 372 (2024).
[10] Y.-S. Kim, H. Hong, T. Hong, S.-H. Choi, K.-B. Chung, and J.-S. Park, Attaining quantitatively fewer defects in close-packed InGaZnO synthesized using atomic layer deposition, Appl. Surf. Sci. **664**, 160242 (2024).
[11] S. Jeong, S. Jang, H. Han, H. Kim, and C. Choi, C-axis aligned crystalline indium-gallium-zinc oxide (CAAC-IGZO) and high-k charge trapping film for flash memory application, J. Alloy. Compd. **888**, 161440 (2021).
[12] H. Kunitake et al., A c-Axis-Aligned Crystalline In-Ga-Zn Oxide FET With a Gate Length of 21 nm Suitable for Memory Applications, IEEE J. Electron Devices Soc. **7**, 495 (2019).
[13] Y. Kobayashi et al., Electrical characteristics and short-channel effect of c-axis aligned crystal indium gallium zinc oxide transistor with short channel length, Jpn. J. Appl. Phys. **53**, 04EF03 (2014).
[14] H. Han, S. Jang, D. Kim, T. Kim, H. Cho, H. Shin, and C. Choi, Memory Characteristics of Thin Film Transistor with Catalytic Metal Layer Induced Crystallized Indium-Gallium-Zinc-Oxide (IGZO) Channel, Electronics **11**, 53 (2022).
[15] Z. Wang, N. Lu, J. Wang, D. Geng, L. Wang, and G. Yang, Charge Trapping and Emission Properties in CAAC-IGZO Transistor: A First-Principles Calculations, Materials **16**, 6 (2023).
[16] S. Yamazaki, J. Koyama, Y. Yamamoto, and K. Okamoto, 15.1: Research, Development, and Application of Crystalline Oxide Semiconductor, SID Symposium Digest of Technical Papers **43**, 183 (2012).
[17] S. Matsuda et al., *30-Nm-Channel-Length c-Axis Aligned Crystalline In-Ga-Zn-O Transistors with Low off-State Leakage Current and Steep Subthreshold Characteristics*, in *2015 Symposium on VLSI Technology (VLSI Technology)* (2015), pp. T216–T217.
[18] T. Hong, Y.-S. Kim, S.-H. Choi, J. H. Lim, and J.-S. Park, Exploration of Chemical Composition of In–Ga–Zn–O System via PEALD Technique for Optimal Physical and Electrical Properties, Advanced Electronic Materials **9**, 2201208 (2023).
[19] T. Masashi and Y. Shunpei, CAAC-Oxide Semiconductor Material and its Applications, Proceedings of the International Display Workshops (CD-ROM) **22nd**, 1 (2015).
[20] D. Matsubayashi et al., *20-Nm-Node Trench-Gate-Self-Aligned Crystalline In-Ga-Zn-Oxide FET with High Frequency and Low off-State Current*, in *2015 IEEE International Electron Devices Meeting (IEDM)* (2015), p. 6.5.1-6.5.4.
[21] S.-D. Huang, C. Shang, X.-J. Zhang, and Z.-P. Liu, Material discovery by combining stochastic surface walking global optimization with a neural network, Chem Sci **8**, 6327 (2017).
[22] X.-J. Zhang, C. Shang, and Z.-P. Liu, Pressure-induced silica quartz amorphization studied by iterative stochastic surface walking reaction sampling, Phys Chem Chem Phys **19**, 4725 (2017).
[23] C. Shang, X.-J. Zhang, and Z.-P. Liu, Stochastic surface walking method for crystal structure and phase transition pathway prediction, Phys Chem Chem Phys **16**, 17845 (2014).
[24] S.-D. Huang, C. Shang, P.-L. Kang, X.-J. Zhang, and Z.-P. Liu, LASP: Fast global potential energy surface exploration, WIREs Computational Molecular Science **9**, e1415

*Contact author: yefeil@fudan.edu.cn;
zpliu@ fudan.edu.cn

(2019).
[25] G. Kresse and J. Furthmüller, Efficient iterative schemes for ab initio total-energy calculations using a plane-wave basis set, Phys Rev B Condens Matter **54**, 11169 (1996).
[26] P. E. Blöchl, Projector augmented-wave method, Phys Rev B Condens Matter **50**, 17953 (1994).
[27] G. Kresse and D. Joubert, From ultrasoft pseudopotentials to the projector augmented-wave method, Physical Review B **59**, 1758 (1999).
[28] H. J. Monkhorst and J. D. Pack, Special points for Brillouin-zone integrations, Phys. Rev. B **13**, 5188 (1976).
[29] J. P. Perdew, K. Burke, and M. Ernzerhof, Generalized Gradient Approximation Made Simple, Phys Rev Lett **77**, 3865 (1996).
[30] J. Heyd, G. E. Scuseria, and M. Ernzerhof, Hybrid functionals based on a screened Coulomb potential, J. Chem. Phys. **118**, 8207 (2003).
[31] S. Smidstrup et al., QuantumATK: an integrated platform of electronic and atomic-scale modelling tools, J. Phys.: Condens. Matter **32**, 015901 (2019).
[32] M. J. van Setten, M. Giantomassi, E. Bousquet, M. J. Verstraete, D. R. Hamann, X. Gonze, and G.-M. Rignanese, The PseudoDojo: Training and grading a 85 element optimized norm-conserving pseudopotential table, Computer Physics Communications **226**, 39 (2018).
[33] C. J. Bartel, Review of computational approaches to predict the thermodynamic stability of inorganic solids, J Mater Sci **57**, 10475 (2022).
[34] K. Nomura, H. Ohta, K. Ueda, T. Kamiya, M. Hirano, and H. Hosono, Thin-Film Transistor Fabricated in Single-Crystalline Transparent Oxide Semiconductor, Science **300**, 1269 (2003).
[35] Y. Yamada et al., Single crystalline In–Ga–Zn oxide films grown from c-axis aligned crystalline materials and their transistor characteristics, Jpn. J. Appl. Phys. **53**, 091102 (2014).
[36] J. T. Jang, S.-J. Choi, D. M. Kim, and D. H. Kim, The Calculation of Negative Bias Illumination Stress-Induced Instability of Amorphous InGaZnO Thin-Film Transistors for Instability-Aware Design, IEEE Transactions on Electron Devices **65**, 1002 (2018).
[37] H. Li, Y. Guo, and J. Robertson, Oxygen vacancies and hydrogen in amorphous In-Ga-Zn-O and ZnO, Phys. Rev. Materials **2**, 074601 (2018).
*Contact author: yefeil@fudan.edu.cn;
zpliu@ fudan.edu.cn
[38] S. Hong, S. Lee, M. Mativenga, and J. Jang, Reduction of Negative Bias and Light Instability of a-IGZO TFTs by Dual-Gate Driving, IEEE Electron Device Letters **35**, 93 (2014).
[39] T. Hiramatsu, M. Nakashima, E. Kikuchi, N. Ishihara, M. Tsubuku, K. Dairiki, and S. Yamazaki, Correlation between crystallinity and oxygen vacancy formation in In–Ga–Zn oxide, Jpn. J. Appl. Phys. **55**, 021203 (2016).
[40] B. Cordero, V. Gómez, A. E. Platero-Prats, M. Revés, J. Echeverría, E. Cremades, F. Barragán, and S. Alvarez, Covalent radii revisited, Dalton Trans. 2832 (2008).
[41] J. Shi, J. Zhang, L. Yang, M. Qu, D.-C. Qi, and K. H. L. Zhang, Wide Bandgap Oxide Semiconductors: from Materials Physics to Optoelectronic Devices, Advanced Materials **33**, 2006230 (2021).
[42] R. Quhe et al., Simulations of Quantum Transport in Sub-5-nm Monolayer Phosphorene Transistors, Phys. Rev. Appl. **10**, 024022 (2018).
[43] Z. Ni, Q. Liu, K. Tang, J. Zheng, J. Zhou, R. Qin, Z. Gao, D. Yu, and J. Lu, Tunable Bandgap in Silicene and Germanene, Nano Lett. **12**, 113 (2012).
[44] S. B. Desai et al., MoS2 transistors with 1-nanometer gate lengths, Science **354**, 99 (2016).
[45] H. Yin, H. Yang, S. Xu, D. Pan, J. Xu, K. Chen, and L. Yu, High Performance Si Nanowire TFTs With Ultrahigh on/off Current Ratio and Steep Subthreshold Swing, IEEE Electron Device Letters **41**, 46 (2020).